The Eurasia Proceedings of Science, Technology,
Engineering & Mathematics (EPSTEM)
ISSN: 2602-3199

The Eurasia Proceedings of Science, Technology, Engineering & Mathematics (EPSTEM), 2024

Volume 32, Pages 389-399

IConTES 2024: International Conference on Technology, Engineering and Science

Simulation Study of Electronic Band Diagram Engineering and Electrical Parameters to Boost the Photovoltaic Performance of Novel Rb_2PtI_6 Double Perovskite Solar Cell

Souheyla Mamoun
Abou Bekr Belkaid University of Tlemcen

Abdelkrim El-Hasnaine Merad
Abou Bekr Belkaid University of Tlemcen

Amina Benmansour
Abou Bekr Belkaid University of Tlemcen

Abstract: It was shown recently that the double perovskite Rb_2PtI_6 exhibits excellent electronic and optical properties that are relevant for photovoltaic applications in particular. Herein, we report deep simulation results of a novel high-performance lead-free halide double perovskite solar cell (PSC) with the architecture FTO/ZnSe/Rb_2PtI_6/$MoSe_2$/C. The thicknesses of all layers such as: FTO, hole transport layer (HTL), Rb_2PtI_6 absorber and electron transport layer (ETL) for the device were optimized. The role of electronic band diagram engineering is demonstrated to be essential for the photovoltaic performance of the solar cell. Moreover, the effects of capacitance (C-V), Mott–Schottky (M-S) characteristics, generation and recombination rates, series resistance (R_s) and shunt resistance (R_{sh}) on the current-voltage characteristics (J-V), and quantum efficiency (QE) are analyzed. Our obtained results shows that this best proposed Rb_2PtI_6-based device can serve as a potential eco-friendly high efficiency solar cell candidate due to the chemical stability and non-toxicity of its active layer. The best obtained efficiency PCE reaches $20.54\,\%$, with short circuit current density J_{SC} of $34.41\ mA/cm^2$, open circuit voltage V_{oc} of $0.79\ V$ and fill factor FF of $75.8\ \%$ compared to the initial PCE of $12.94\,\%$. To validate our results, we compared the simulation outcomes with other similar double PSC cells previously published. Good agreement is obtained with experimental and simulation studies.

Keywords: Lead-free halide double perovskite solar cells based on Rb_2PtI_6, band gap diagram, Generation and recombination rates, Series resistance (R_s), Shunt resistance (R_{sh}).

Introduction

In the purpose to enhance the power conversion efficiency (PCE) of photovoltaic (PV) solar cells (SC) in a hand and preserve the ecologic system for future generation from polluted materials in the other hand, several experimental and theoretical studies have been published. Thus, a scientific and ecologic race to search and use appropriate materials appeared. Recently, halide perovskites (HP) ABX_3 are in the top of this race due to their attractive properties such as tunable band gap (Huang et al., 2017). Strong light absorption (Yue et al., 2016). And high carrier mobilities (Sun et al., 2021**)**. To have more ideas about the whole perovskites' studies published we can refer to the following review papers: Jodlowski et al. (2018),Yin et al. (2019), Lu. et al. (2020), Zhao et al. (2021), Nair et al. (2022).

In some studies, the cation A (who was formed by the methylammonium $[CH_3NH_3]^+$(MA^+) in the earlier studies of HP) was substituted partially or completely by another organic cation formamidinium $[HC(NH_2)_2]^+$(FA^+) (Zhang et al., 2018; Zheng et al., 2022). And inorganic ones like cesium (Cs^+), Gallium (Ga), potassium (K^+) and rubidium (Rb^+) (Saliba et al., 2016;Park et al., 2017;Ono et al., 2017).

- Selection and peer-review under responsibility of the Organizing Committee of the Conference

In others studies, the anion B (who was formed by the toxic element lead (Pb^{2+}) in the earlier studies of HP) has been also partially or completely replaced by other elements like: silver (Ag^{+}) (Abdi-Jalebi et al., 2016). Copper Cu^{+}(Shahbazi et al., 2017). Tin (Sn^{2+}) (Fujihara et al., 2017**)**. Germanium (Ge^{2+}) (Kanoun et al., 2019**)**. Antimony (Sb^{3+}) (Boopathi et al., 2017). Bismuth (Bi^{3+}) (Jin et al., 2020). It seems that this effect responds to this need but it affects negatively the stability: the mixed organic-inorganic cation (HP) structures formed are vulnerable to degradation upon exposure to light, high temperature and humidity (Wei et al., 2020).

However, in inorganic halide double perovskite structures (IHDP) A_2BX_6, and especially in the vacancy ordered ones, this main problem is taken off due to the strong covalency in the cluster $[BX_6]^{2-}$(Bartel et al., 2019). And especially in platinum (Pt) based ones (Suzuki et al., 2021). It is shown that the rotation angles θ of the PtX_6 octahedra are non-zero. For a given A-site cation, θ increases from Cl to Br to I while for a given halide anion, θ decreases from K to Rb to Cs. It is found that the band gap values increase when the halogen element X is varied from iodide I, to bromide Br to chloride Cl (Cai et al., 2017; Faizan et al., 2021). Also, it is proved that iodide based double perovskite are the most efficiency (Kumar et al., 2021**)**.

It was proven by ab initio calculation Cai et al. (2017), Zhao et al. (2021), (Suzuki et al., 2021) that the two vacancy ordered IHDP Cs_2PtI_6 and Rb_2PtI_6 are stables (formation enthalpy equal to -0,97 and - 0.92 eV/atom respectively), have suitable band gap (1.4 eV and 1.3 eV in the cubic structure respectively), their absorption coefficients are of the order of 10^4–10^5 cm^{-1}. Indeed, employing the spectroscopically limited maximum efficiency as a metric for quantifying the photovoltaic performance, these iodides compounds are found to be promising absorbers in solar cells.

Since recently, a new promising solar cell based on the vacancy ordered IHDP Cs_2PtI_6 has been synthetized and experimentally tested by Schwartz et al. (2020) it has an excellent stability and oxidation resistance, high absorption coefficient (4×10^5 cm^{-1} superior than $MAPbI_3$'one $10^5 cm^{-1}$) and long carrier life time (superior than 2μs as long as that of $MAPbI_3$). The PCE of their adopted structure FTO/CdS/Cs_2PtI_6(10-15 μm)/ElectroDAG440B/Cu is about 10.7% and can enhance to 13.88 % when ethylene diamine EDA (a chemical treatment) is added.

Using SCAPS-1D software **(**Burgelman et al., 2021). Cs_2PtI_6 was also theoretically studied by Shamna et al. (2022), AbdElaziz et al. (2022), and Amjad et al. (2023). They showed that the PCE of their optimized structure FTO/ZnO/Cs_2PtI_6/MoO_3/C, FTO/WS_2/Cs_2PtI_6($0.4\ \mu m$)/Cu_2O/C and FTO/SnO_2/Cs_2PtI_6($0.4\ \mu m$)/MoO_3/C can reach 20.45 %, 22.4 % and 23.52 % respectively.

Then, as Cs_2PtI_6, Rb_2PtI_6 can be also an effective candidate for lead-free photovoltaic materials whereas, to our best knowledge, it has not been used in any theoretical or experimental solar cell study. In this context, we aim to investigate numerically, for the first time, the photovoltaic performances of a novel solar cell architecture based on the vacancy ordered IHDP Rb_2PtI_6 as absorber using the SCAPS-1D code (Burgelman et al., 2021**)**.

In this study, we sandwich the IHDP Rb_2PtI_6 between ZnSe used as electron transport layer (ETL) and $MoSe_2$ used as hole transport layer (HTL) and we try to ameliorate the PV performance of this initial device by the optimization of the thicknesses of all layers. We extend the study to the analysis of the effects of capacitance (C-V), Mott–Schottky (M-S) characteristics, generation and recombination rates, series resistance (R_s) and shunt resistance (R_{sh}) on the current-voltage characteristics (J-V).

Method

We used SCAPS-1D code (Burgelman et al., 2021**)**. Which is based theoretically on the fundamental equations: Poisson's equation (1) and continuity equation for holes and electrons equation (2):

$$\frac{d^2\psi}{dx^2} = \frac{e}{\varepsilon_0\varepsilon_r}\left[p(x) - n(x) + N_D - N_A + \rho_p - \rho_n\right] \tag{1}$$

Where ψ is electrostatic potential, n and p are electron and hole concentrations, ε_0 is vacuum and ε_r is relative permittivity, N_D and N_A are donor and acceptor doping density, ρ_n, ρ_p are electrons and holes distribution,

$$\frac{dJ_p}{dx} = \frac{dJ_n}{dx} = G - R \tag{2}$$

Where G is generation rate and R is recombination rate, J_p and J_n are holes and electron current densities.

Carrier transport occurs according to the following drift and diffusion equations:

$$J_n = \mu_n n \frac{d\psi}{dx} + D_n \frac{dn}{dx} \tag{3}$$

$$J_p = \mu_p p \frac{d\psi}{dx} + D_p \frac{dp}{dx} \tag{4}$$

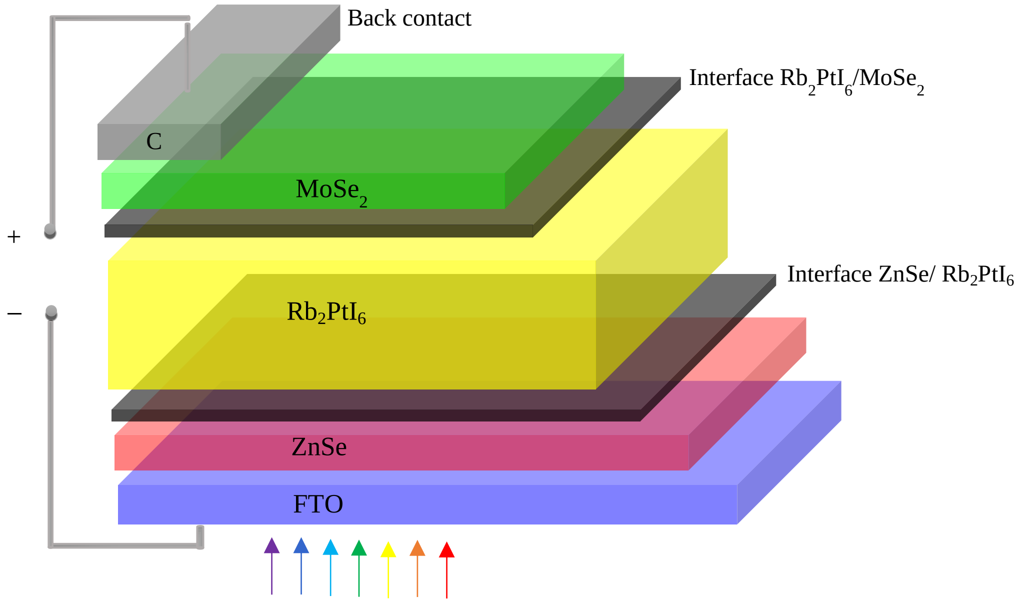

Figure 1. Architecture of the adopted device

The device architecture model FTO/ZnSe/Rb_2PtI_6/$MoSe_2$/C is depicted in (Figure1). The zinc selenide ZnSe is used as an electron transport layer (ETL). The absorber or active layer is formed by the double perovskite Rubidium (IV) platinum iodide Rb_2PtI_6 material. The Molybdenum diselenide $MoSe_2$ is used as a hole transport layer (HTL). The Fluorine-doped tin oxide (FTO) is use in the front side and the carbon C is used as contact in the back side.

Our studied device is a n-i-p type, for that, the n part is the ETL, the i part is the absorber and the p part is the HTL. To make our model more realistic, we have added the interface layers: interface (ETL/Rb_2PtI_6) and interface (Rb_2PtI_6/HTL), with a thickness of 5nm and keeping the same physical parameters as those of the perovskite.

We report in (Table 1) the input parameters for $MoSe_2$, Rb_2PtI_6, ZnSe and FTO derived from the literature and also, obtained with our calculations since some parameters of Rb_2PtI_6 are not yet available. For that, we have opted to the theoretical determination of such parameters based on the following equations:

$$N_t = \frac{1}{\sigma \tau V_{th}} \tag{5}$$

$$\mu_{n/p} = \frac{D_{n/p} q}{KT} \qquad 6)$$

$$D_{n/p} = \frac{{l_{n/p}}^2}{\tau} \tag{7}$$

Where N_t is the defect density, $\mu_{n/p}$ is the electron/hole mobility, $D_{n/p}$ is the electron/hole diffusion coefficient, K is Boltzmann’s constant, τ is the charge carrier lifetime, $l_{n/p}$ is the electron/hole diffusion length; σ is the capture cross-section of electron/hole and V_{th} is the thermal velocity of electron/hole. Also, the absorber layer effective conduction band density of states, N_c and effective valence band density of states, N_v are determined using the two following expressions:

$$N_c = 2\left(\frac{2\pi m_n^* KT}{h^2}\right)^{\frac{3}{2}} \text{ and } N_v = 2\left(\frac{2\pi m_p^* KT}{h^2}\right)^{\frac{3}{2}} \qquad 8)$$

Where m_n^* and m_p^* are the effective masses of electrons and holes, respectively.

We notice that all initial layer's thicknesses are set to be 0.1μm and the simulation is done under the following physical conditions: solar illumination of $AM\ 1.5\ G$, with an intensity of $100\ mWcm^{-2}$, temperature of $300\ K$, and working frequency of $10^6 Hz$.

Table 1. The input parameters of the adopted device

Input parameter	$MoSe_2$	Rb_2PtI_6	ZnSe	FTO
Band gap, E_g (eV)	1.35[a]	1.3[b]	2.81[f]	3.5[g]
Affinity, χ (eV)	4.05[a]	4.43[c]	4.09[f]	4[g]
Relative Dielectric permittivity, ε_r	11.9[a]	4.34[d]	8.6[f]	9[g]
CB effective density of states, N_c (cm^{-3})	2.8×10^{19}[a]	7.5×10^{18}[c]	2.2×10^{18}[f]	9.2×10^{18}[g]
VB effective density of states, N_v (cm^{-3})	2.65×10^{19}[a]	3.5×10^{19}[c]	1.8×10^{19}[f]	1.8×10^{19}[g]
Electron mobility, μ_n $(cm^2V^{-1}s^{-1})$	1450[a]	0.65[e]	400[f]	20[g]
hole mobility, μ_p $(cm^2V^{-1}s^{-1})$	50[a]	3.25[e]	100[f]	10[g]
Electron effective mass, m_n^*	-	0.45[b]	-	-
hole effective mass, m_p^*	-	1.245[b]	-	-
Density of n-type doping, N_D (cm^{-3})	0	0	10^{18}[f]	10^{19}[g]
Density of p-type doping, N_A (cm^{-3})	4×10^{18}[a]	10^{15}[c]	0	0
Density of defect, N_t (cm^{-3})	10^{14}[a]	3.5×10^{15}[c]	10^{15}[f]	10^{15}[g]

[a]data from Teyou- Ngoupo et al. (2022)
[b]data from Cai et al. (2017), [c] our calculations, [d] from Zhao et al.(2021),[e] from Yang (2019)
[f]data from (Owolabi J.A. et al. 2020)
[g]data from (Jahantigh et al. 2019)

Results and Discussion

Optimization of the Device Layers Thicknesses

Since the thickness of each layer of the device is critical to the overall photovoltaic performance of the device, the thicknesses of the FTO, HTL, absorber and ETL of the initial device were optimized. In this step, our strategy of optimization is started for FTO/ZnSe/Rb_2PtI_6/$MoSe_2$/C and is preceded in such the way: The optimization was done sequentially by varying the thickness of a particular layer while keeping the thickness of the remaining layers constant. In this manner, each layer was investigated in turn until a maximum PCE was achieved.

For instance, for the initial SC FTO$(0.1\ \mu m)$/ZnSe$(0.1\ \mu m)$/$Rb_2PtI_6$$(0.1\ \mu m)$/$MoSe_2$$(0.1\ \mu m)$/C) which has initially an $PCE = 12.94$ % for $R_s = 0\ \Omega$, the thickness optimization was carried out as follows: first, the absorber thickness was varied from 0.1 to 2 μm until a maximum PCE was obtained, while the thicknesses of the HTL, ETL, and FTO were kept constant at $0.1\ \mu m$. The best absorber thickness was determined to be 1.2 μm ($PCE = 20.54$ %), after which it was kept constant at this value. The ETL and FTO thicknesses were kept constant, while the thickness of the HTL was varied from 0.01 to 2 μm until an optimum value was attained at 0.04 μm ($PCE = 20.54$ %).

Likewise, the ETL thickness was varied from 0.01 to 2 μm, while the absorber, HTL and FTO thicknesses were kept constant. The optimum ETL thickness was found to be $0.06\ \mu m$ ($PCE = 20.54$ %). Finally, the FTO thickness was optimized by varying its value between 0.01 to 2 μm, and the optimum thickness was determined to be 0.01 μm ($PCE = 20.54$ %).

Then, the optimized SC is: FTO$(0.01\ \mu m)$/ZnSe$(0.06\ \mu m)$/$Rb_2PtI_6$$(1.2\ \mu m)$/$MoSe_2$$(0.04\ \mu m)$/C gives an PCE of 20.54 %. Figure 2 shows the PV performance and quantum efficiency (QE) comparison between the initial and obtimized simulated FTO/ZnSe/Rb_2PtI_6/$MoSe_2$/C structure. The initial solar cell (SC) provides PCE of 12.94 %, J_{SC} of 19.39 mA/cm^2, V_{oc} of 0.79 V, and FF of 87.54 % with QE near 360 nm 360, which is in the UV range. Upon optimizing the thicknesses of FTO, HTL, perovskite and ETL, we have obtained a higher performance: PCE of 20.54 %, J_{SC} of 34.41 mA/cm^2, V_{oc} of 0.79 V and FF of 75.8 % with about 98 % QE from 100 nm to 800 nm, which covers the UV and the visible range.

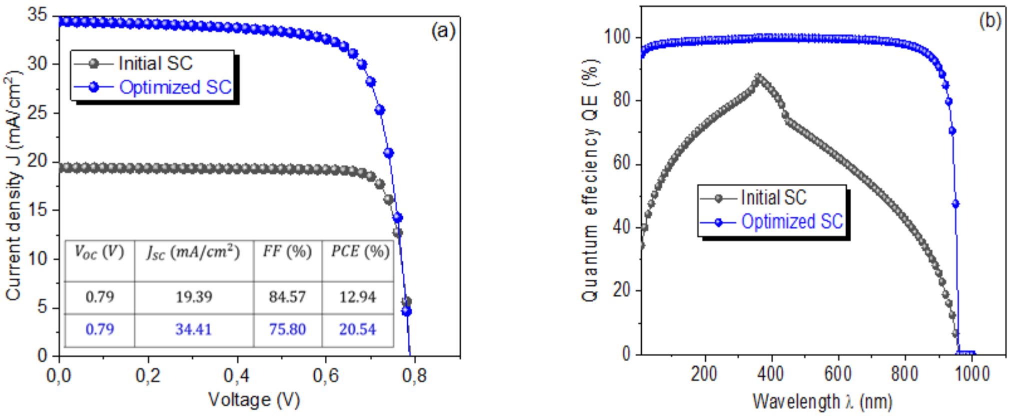

V_{oc} (V)	J_{sc} (mA/cm^2)	FF (%)	PCE (%)
0.79	19.39	84.57	12.94
0.79	34.41	75.80	20.54

Figure 2. a) J-V characteristic and b) QE versus wavelength of FTO/ZnSe/Rb_2PtI_6/$MoSe_2$/C solar cell (SC).

Energy Band Diagram

In order to achieve a higher level of efficiency, the hole transport layer (HTL) and electron transport layer (ETL) must have band gap edges that correspond with the valence band maximum (VBM) and the conduction band minimum (CBM) of the active layers. (Figure 3.a) illustrate the band gap alignment of ZnSe, MoSe2 and Rb_2PtI_6, as well as the back and front device contacts. The lowest unoccupied molecular orbital (LUMO) of ZnSe (ETL) is in excellent alignment with the conduction band of Rb_2PtI_6. Likewise, the highest occupied molecular orbital (HOMO) of $MoSe_2$ (HTL) is well-aligned with the valence band level of an absorbing material

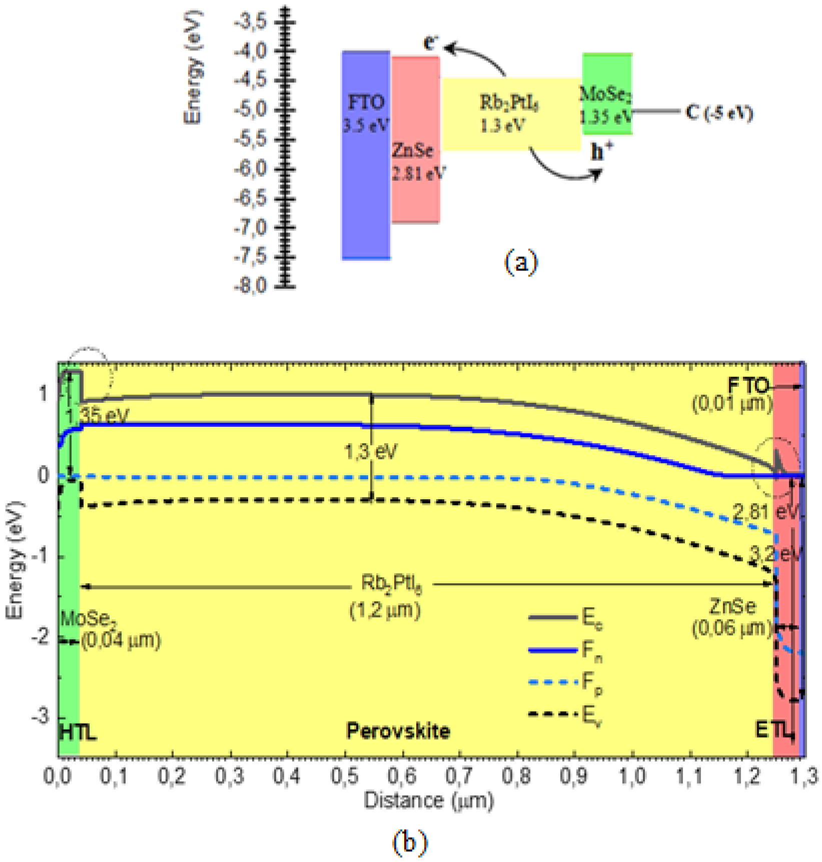

Figure 3. a) Energy level diagram b) conduction and valence energies of the optimized device.

The proper alignment of these energy levels is crucial for the photovoltaic performance of PSCs. Indeed, when light is absorbed, electrons are generated and injected into the conduction band of the ETL, while holes are simultaneously transported to the HTL. Then, electrons and holes are gathered at their corresponding front and back metal contacts. The energy band mismatch at the interfaces between ETL/Rb_2PtI_6 and Rb_2PtI_6/HTL has a significant impact on the device performance parameters. The characteristics of these interfaces exert control over the consequences of interfacial recombination (Sabbah et al., 2022). Therefore, it is necessary to perform precise tuning of the electronic characteristics of ETL and HTL materials. (Sabbah et al., 2022)

According to Ravidas et al. (Ravidas et a 2023). When the valence band offset (VBO) is positive, the spike is established at the absorber/HTL interface. Conversely, when the VBO is negative, a cliff is created at the absorber/HTL interface as shown in (Figure 3.b). The cliff does not obstruct photo-generated hole flow toward a back metal contact (C). However, the activation energy (E_a) for carrier recombination becomes lower than band gap of the absorber E_g (Rb_2PtI_6) and E_a is expressed by E_g (Rb_2PtI_6) - |VBO|. Consequently, a decrease in E_a due to the negative VBO elevates the interface recombination (Ravidas et al. 2023). The VBO at the $MoSe_2/Rb_2PtI_6$ interface is -0.37 eV which is sufficiently small to allow the holes to travel smoothly towards electrodes. When the CBO is positive, the spike is created at the ETL/ absorber interface and when the CBO is negative, the cliff is established at the ETL/ absorber interface (Agha et al., 2022). As illustrated in the inset of (Figure 3.b). The CBO at the Rb_2PtI_6/ZnSe interface is positive; it is about 0.31 eV.

Effect of Generation and Recombination Rate

Carrier generation describes the processes by which electrons gain energy and move from the valence band to the conduction band, producing two mobile carriers (creation); while recombination describes the processes by which an electron in the conduction band loses energy and reoccupies the energy state of an electron hole in the valence band.

Figure 4 illustrates the carrier generation and recombination rates in our model cell at different depths, ranging from 0.0 to 1.3 µm. According to the results, the generation rate of the device reached the peak of 1.447×10^{22} cm^3.s at 1.25 µm. This peak value is considered very higher compared to other solar devices such as $ITO/C60/CsSnBr_3/Cu_2O/Au$ structure which demonstrated the highest generation rate of 0.7×10^{22} cm^3.s in its class (Dar et al. 2024).

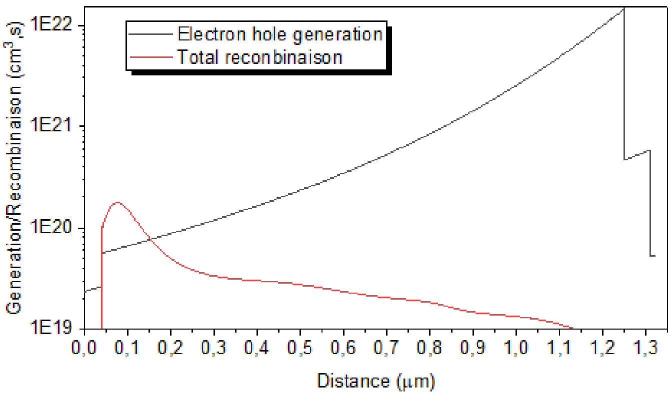

Figure 4. Effect of generation and recombination rate

Effect of Capacitance and Mott-Schotteky

Figure 5 illustrates the variation of the capacitance characteristics as a function of a voltage between -0.8 and 0.8 V. The numerical calculations were performed at a fixed frequency of 1 MHz. The capacitance increases nonlinearly as the voltage increases up to the value of 0.6 V. Beyond this value, the capacitance undergoes an exponential expansion. Normally, we would expect the capacitance to eventually reach its saturation point. It is well known in semiconductor device physics that the Mott-Schotteky (M-S) plot describes the inverse square of the capacitance, given in (Figure 6), versus the potential. The relationship between the capacitance (C), the built-in potential V_{bi} and the doping density (N_D) of the semiconductor is expressed by the following equation:

$$\frac{1}{C^2} = \frac{2\left(V - V_{bi} - \frac{KT}{q}\right)}{q\epsilon_r\epsilon_0 N_D} \tag{9}$$

Where V is the applied voltage and C is the capacitance per unit area.

This equation is used for the calculation of the doping density (N_D) of the semiconductor, while the extrapolation of the intercept can be used to derive the built-in potential (V_{bi}) (Otoufi et al., 2020). The V_{bi} obtained for the considered structure is equal to 1 V as shown in (Figure 6).

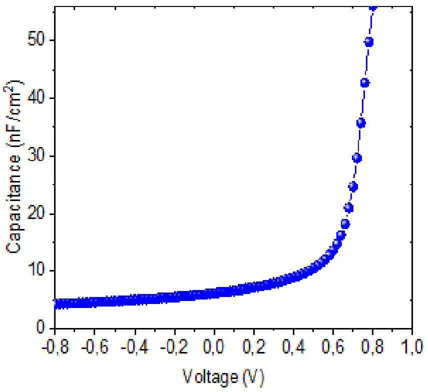

Figure 5. Effect of capacitance

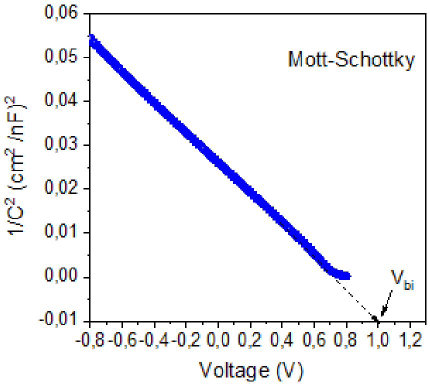

Figure 6. Effect of Mott-Schotteky

Effect of Series and Shunt Resistances

Series resistance (R_s) is due to factors such as ohmic contacts, metallic contacts, ITO sheet resistance, contact resistance inside the cell, and manufacturing imperfections. While, shunt resistance (R_{sh}) results from factors such as crystallographic defects, pinholes in the absorber layer, grain boundaries and the preparation process. R_{sh} is created due to alternating current paths for photogenerated charge carriers, which are provided by various charge recombination pathways in PSCs. The Shockley equation illustrates the relationship between the J-V characteristics of the cell and the resistances.

- For R_s, the Shockley equation is defined as follows:

$$J = J_{ph} - J_0 exp\left[\frac{q(V+IR_s)}{\eta KT}\right] \tag{10}$$

- For R_{sh}, the Shockley equation is defined as follows:

$$J = J_{ph} - J_0 exp\left[\frac{qV}{\eta KT}\right] - \frac{V}{R_{sh}} \tag{11}$$

Where J_{ph} is the photocurrent density, J_0 is reverse saturation current density, V is the output voltage and η is diode ideality factor.Figure 7 shows the contour plot of the variation of the photovoltaic parameters with resistances R_s and R_{sh}. As illustrated, the increase of R_s leads to the decrease of PCE, while the increase of R_{sh} leads to the increase of PCE. Therefore, R_s has a negative effect of the solar cell performance, while R_{sh} has a positive effect. The PCE reaches the maximum value of 20.60 % for very low R_s and very high R_{sh}.

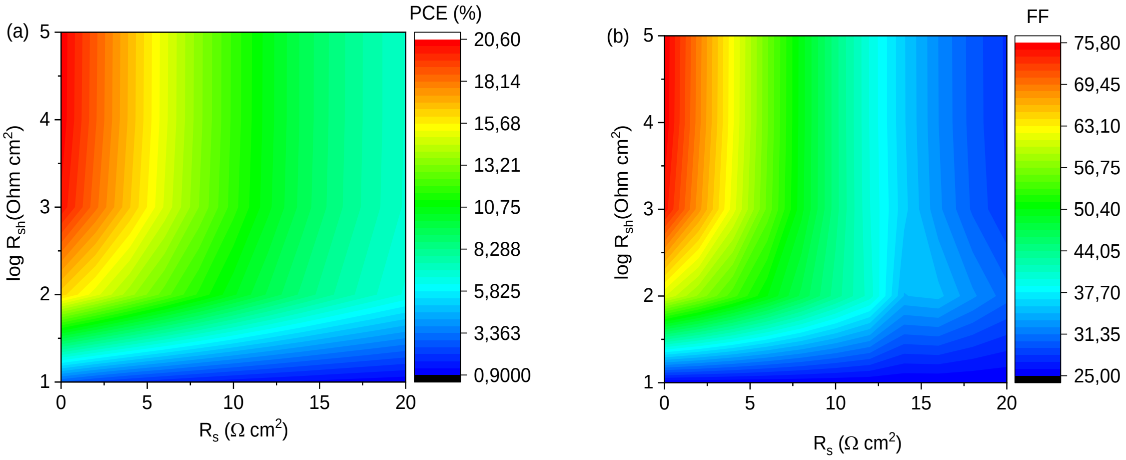

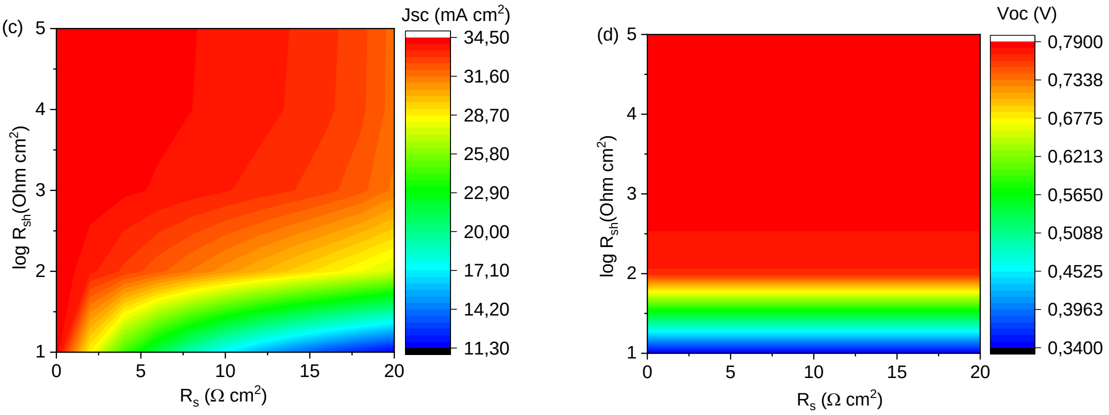

Figure 7. Contour plot of the effect of series and shunt resistances on the PV parameters of the solar cell: a) PCE, b)PCE, c) J_{SC} and d) V_{oc}

Comparison of Our PV Parameters and Others Studies

Since the active layer of our studied device Rb_2PtI_6 is from the same IHDP family as Cs_2PtI_6, we compare the photovoltaic (PV) characteristics of our predicted solar cell based on Rb_2PtI_6 to other ones based on Cs_2PtI_6 where experimental and numerical data are available. We summarized the finding results in (Table 2).

Table 2. PV characteristics of our optimized solar cell compared with other IHDP solar cells. The values between parenthesis are the layers' thicknesses given in ($\boldsymbol{\mu m}$).

Structure	V_{oc} (V)	J_{sc} (mA/cm^2)	FF (%)	PCE (%)	R_s $(\Omega\, cm^2)$	R_{sh} $(\Omega\, cm^2)$	Used Method
FTO (0.01)/ ZnSe(0.06)/ Rb_2PtI_6 (1.2)/$MoSe_2$(0.04)/C [a]	0.79[a]	34.41[a]	75.80[a]	20.54[a]	0	0	SCAPS-1D
	0.79[a]	34.41[a]	75.75[a]	20.53[a]	0.01	10^5	
	0.79[a]	34.41[a]	75.62[a]	20.49[a]	0.01	10^4	
	0.79[a]	34.38[a]	71.02[a]	19.49[a]	1	4.2×10^3	
	0.79[a]	15.15[a]	25.17[a]	03.01[a]	50	10^4	
	0.79[a]	33.47[a]	35.71[a]	09.42[a]	14	10^4	
FTO/CdS (0.08-0.1)/ Cs_2PtI_6 (10-15)/ElectroDAG 440B/Cu [b]	0.90[b]	19.83[b]	59.85[b]	10.70[b]	14	-	Exp
FTO/CdS (0.08-0.1)/ Cs_2PtI_6 (10-15)/ElectroDAG 440B/Cu with EDA traitment [b]	1.07[b]	19.84[b]	65.03[b]	13.88[b]			
FTO (0.5)/WS_2/ Cs_2PtI_6 (0.4)/Cu_2O /C [c]	1.3[c]	28.15[c]	61.00[c]	22.4[c]	14	-	SCAPS-1D
FTO (0.5)/SnO_2(0.01)/ Cs_2PtI_6 (0.4)/MoO_3(0.024)/C [d]	1.11[d]	26.95[d]	79.90[d]	24.10[d]	0.01	10^4	SCAPS-1D
	1.11[d]	26.95[d]	78.07[d]	23.52[d]	1	4.2×10^3	
	1.11[d]	21.06[d]	25.57[d]	06.03[d]	50	10^4	
FTO/ZnO / Cs_2PtI_6 /MoO_3 /C [e]	1.40[e]	16.11[e]	90.01[e]	20.45[e]	0	0	SCAPS-1D

[a] our optimized SC based on Rb_2PtI_6

[b] experimental SC based on Cs_2PtI_6 (Schwartz et al., 2020)

[c] simulated SC based on Cs_2PtI_6 (AbdElAziz et al., 2022)

[d] simulated SC based on Cs_2PtI_6 (Amjad et al., 2023)

[e] simulated SC based on Cs_2PtI_6 (Shamna et al., 2022)

The PCE ranges from 6.03 % (FTO/ZnO/Cs_2PtI_6/MoO_3/C) to 24.1 % (FTO/SnO_2/Cs_2PtI_6/MoO_3/C) with Cs_2PtI_6 perovskite. We can see that the negative effect of the series resistance R_s is remarkable in this case because it drastically decreases the PCE of the solar cell. Compared to these similar solar cells, our results for FTO/SnO_2/Rb_2PtI_6/$MoSe_2$/C show good agreement with the PCE of 20.54 %. We notice that SCAPS-1D PV results reported in the references given in Table 2, the authors performed their obtained devices with the study of the effect of acceptor density N_A and defect density N_t of the active layer. We expect, then, a clear improvement in PCE of our predicted device if we also take into account these later effects.

Conclusion

This paper provided deep simulation results of a novel high-performance solar cell based on the double perovskite: Rubidium (IV) platinum iodide Rb_2PtI_6. Our adopted architecture is FTO/ZnSe/Rb_2PtI_6/$MoSe_2$/C. The optimal performance of our proposed cell was achieved by varying the thicknesses of all layers such as: FTO, hole transport layer (HTL), Rb_2PtI_6 absorber and electron transport layer (ETL). We have presented a valuable insight on how the electronic band diagram engineering is fundamental for the photovoltaic performance of the solar cell. Moreover, the effects of capacitance (C-V), Mott–Schottky (M-S) characteristics, generation and recombination rates, series resistance (R_s) and shunt resistance (R_{sh}) are analyzed. The best obtained efficiency PCE reaches 20.54 % and we expect, even more improvement in PCE if we investigate the effect of acceptor density, and defct concentration of the absorber layer.

The QE of our redicted devive is 98 % from $100\ nm$ to $800\ nm$, which covers the UV and the visible range. Our findings shows that our proposed Rb_2PtI_6-based device can serve as a potential eco-friendly high efficiency solar cell candidate due to the chemical stability and non-toxicity of its active layer. Good agreement is obtained with available experimental and simulation studies for similar solar cells.

Scientific Ethics Declaration

The authors declare that the scientific ethical and legal responsibility of this article published in EPSTEM Journal belongs to the authors.

Acknowledgements

The authors are thankful to Professor Marc Burgelman and his coworkers at the University of Ghent, Belgium, for providing the SCAPS-1D software used in this study.

Notes

* This article was presented as an oral presentation at the International Conference on Technology, Engineering and Science (www.icontes.net) held in Antalya/Turkey on November 14-17, 2024.

References

AbdElAziz, H. H., Taha, M., El Rouby, W.M.A., Khedr, M.H., & Saad, L. (2022). Evaluating the performance of $Cs_2PtI_{6-x}Br_x$ for photovoltaic and photocatalytic applications using first-principles study and SCAPS-1D simulation. *Heliyon, 8*(10), e10808.

Agha, D.N.Q., & Algwari Q.Th. (2022). The influence of the conduction band engineering on the perovskite solar cell performance. *Results in Optics, 9*(15), 100291.

Amjad, A., Qamar, S., Zhao, C., Fatima, K., Sultan, M., & Akhter, Z. (2023). Numerical simulation of lead-free vacancy ordered Cs_2PtI_6 based perovskite solar cell using SCAPS-1D. *RSC Advances,13*(33), 23211–23222.

Bartel, C.J., Sutton, C., Goldsmith, B.R., Runhai, O., Musgrave, C.B., Ghiringhelli, L.M., & Scheffler, M. (2019). New tolerance factor to predict the stability of perovskite oxides and halides. *Science Advances, 5(2),* eaav0693.

Boopathi, K.M., Karuppuswamy, P., Singh, A., Hanmandlu, C., Lin, L., Abbas, S. A., Chang, C.C, Wang, P.C., Li, G. & Chu, C. W. (2017). Solution-processable antimony-based light-absorbing materials beyond lead halide perovskites. *Journal of Materials Chemistry A, 5*(39), 20843-20850.

Burgelman, M., Decock, K., Niemegeers, A., Verschraegen, J., & Degrave, S. J. F. (2021). *SCAPS manual.* Retrieved from https://scaps.elis.ugent.be/SCAPS%20manual%20most%20recent.pdf

Cai, Y., Xie, W., Ding, H., Chen, Y., Thirumal, K., Wong, L.H., Mathews, N., Mhaisalkar, S.G., Sherburne, M., & Asta, M. (2017). Computational study of halide perovskite-derived a_2bx_6 inorganic compounds: chemical trends in electronic structure and structural stability. *Chemistry of Materials*, *29*(18), 7740−7749.

Dar S.A., & Sengar, B. S. (2024). Analysis of lead free $CsSnBr_3$ based perovskite solar cells utilizing numerical modeling. *Physica Scripta, 99*(6), 065013.

Faizan, M., Bhamu, K. C., Khan, S. H., Murtaza, G., & He, X., (2020). Computational study of defect variant perovskites a_2bx_6 for photovoltaic applications. *arXiv:2002*, 07543.

Fujihara, T., Terakawa, S., Matsushima, T., Qin, C., Yahiro, M., & Adachi, C. (2017). Fabrication of high coverage MASnI 3 perovskite films for stable, planar heterojunction solar cells. *Journal of Materials Chemistry C*, *5*(5), 1121-1127.

Huang, H., Raith, J., Kershaw, S. V., Kalytchuk, S., Tomanec, O., Jing, L., ... & Rogach, A. L. (2017). Growth mechanism of strongly emitting CH3NH3PbBr3 perovskite nanocrystals with a tunable bandgap. *Nature Communications*, *8*(1), 996.

Jahantigh, F., & Safikhani, M. J. (2019). The effect of HTM on the performance of solid-state dye-sanitized solar cells (SDSSCs): A SCAPS-1D simulation study. *Applied Physics A*, *125*(4), 276.

Jin, Z., Zhang, Z., Xiu, J., Song, H., Gatti, T., & He, Z. (2020). A critical review on bismuth and antimony halide based perovskites and their derivatives for photovoltaic applications: recent advances and challenges. *Journal of Materials Chemistry A*, *8*(32), 16166-16188.

Jodlowski, A., Rodríguez-Padrón, D., Luque, R., & de Miguel, G. (2018). Alternative perovskites for photovoltaics. *Advanced Energy Materials*, *8*(21), 1703120.

Kanoun, A.A., Kanoun, M.B., Merad, A.E. & Goumri-Said, S., (2019). Toward development of high-performance perovskite solar cells based on $CH_3NH_3GeI_3$ using computational approach. *Solar Energy 182*, 237-244.

Kumar, N., Rani, J. & Kurchania, R. (2021). A review on power conversion efficiency of lead iodide perovskite-based solar cells. *Materials Today: Proceedings 46,* 5570-5574.

Lu, L., Pan, X., Luo, J., & Sun, Z. (2020). Recent advances and optoelectronic applications of lead-free halide double perovskites. *Chemistry–A European Journal*, *26*(71), 16975-16984.

Nair, S.S., Krishina, L., Trukhanov, A., Thakur, P., & Thakur, A. (2022). Prospect of double perovskite over conventional perovskite in photovoltaic applications. *Ceramics International*, *48*(3), 34128-34147.

Otoufi, M.K., Ranjbar, M., Kermanpur, A., Taghavinia, N., Minbashi, M., Forouzandeh, M., & Ebadi F. (2020). Enhanced performance of planar perovskite solar cells using TiO_2/SnO_2 and TiO_2/WO_3 bilayer structures Roles of the interfacial layers. *Solar Energy*, *208*, 697–707.

Ono, L. K., Juarez-Perez, E. J., & Qi, Y. (2017). Progress on perovskite materials and solar cells with mixed cations and halide anions. *ACS Applied Materials & Interfaces*, *9*(36), 30197-30246.

Owolabi, J.A., Onimisi, M.Y., Ukwenya, J.A., Bature, A.B., & Ushiekpan, U.R. (2020). Investigating the effect of ZnSe (ETM) and Cu_2O (HTM) on absorber layer on the performance of pervoskite solar cell using SCAPS-1D. *American Journal of Physics and Applications 8*, 8-18.

Park, Y. H., Jeong, I., Bae, S., Son, H. J., Lee, P., Lee, J., ... & Ko, M. J. (2017). Inorganic rubidium cation as an enhancer for photovoltaic performance and moisture stability of HC (NH2) 2PbI3 perovskite solar cells. *Advanced Functional Materials*, *27*(16), 1605988.

Ravidas, B. K., Roy, M.K. & Samajdar, D.P. (2023). Investigation of photovoltaic performance of lead-free CsSnI3-based perovskite solar cell with different hole transport layers, first principle calculations and SCAPS-1D analysis. *Solar Energy*, *249*, 163–173.

Sabbah, H., Arayro, J.& Mezher, R. (2022). Numerical simulation and optimization of highly stable and efficient lead-free perovskite $FA_{1-x}Cs_xSnI_3$-based solar cells using SCAPS. *Materials 15*(14), 4761.

Saliba, M., Matsui, T., Seo, J. Y., Domanski, K., Correa-Baena, J. P., Nazeeruddin, M. K., ... & Grätzel, M. (2016). Cesium-containing triple cation perovskite solar cells: improved stability, reproducibility and high efficiency. *Energy & Environmental Science*, *9*(6), 1989-1997.

Schwartz, D., Murshed, R., Larson, H., Usprung, B., Soltanmohamad, S., Pandey, R., Barnard, E.S., Rockett, A., Hartmann, T., Castelli, I.E., & Bansal S. (2020). Air stable, high-efficiency, pt-based halide perovskite solar cells with long carrier lifetimes. *Physica Statu Solidi*, *14*, 2000182.

Shahbazi, S., Tsai, C. M., Narra, S., Wang, C. Y., Shiu, H. S., Afshar, S., ... & Diau, E. W. G. (2017). Ag doping of organometal lead halide perovskites: morphology modification and p-type character. *The Journal of Physical Chemistry C*, *121*(7), 3673-3679.

Shamna, M.S., & Sudheer, K.S. (2022). Device modeling of Cs_2PtI_6-based perovskite solar cell with diverse transport materials and contact metal electrodes: A comprehensive simulation study using solar cell capacitance simulator. *Journal of Photonics for Energy*, *12*(3), 032211.

Sun, P.P., Kripalani, D.R., Chi, W., Snyder, S.A., & Zhou, K. (2021). High carrier mobility and remarkable photovoltaic performance of two-dimensional Ruddlesden–Popper organic–inorganic metal halides $(PA)_2(MA)_2M_3I_{10}$ for perovskite solar cell applications. *Materials Today, 47,* 45-52.

Suzuki, S., & Tsuyama, M., (2021). Structural, electronic, and optical properties of Pt-based vacancy-ordered double perovskites A_2PtX_6 (A = K, Rb, Cs; X = Cl, Br, I) in tetragonal P4/mnc polymorph. *Optical Materials 119,* 111323.

Teyou Ngoupo, A. & Ndjaka, J.M.B. (2022). Performance enhancement of Sb_2Se_3 -based solar cell with hybrid buffer layer and $MoSe_2$ as a hole transport material using simulator device. *Discover Mechanical Engineering*, *1*(1), 5.

Wei, H., Chen, S., Zhao, J., Yu, Z., & Huang, J. (2020). Is formamidinium always more stable than methylammonium?. *Chemistry of Materials*, *32*(6), 2501-2507.

Yang, Z., Yu, Z., Wei, H., Xiao, X., Ni, Z., Chen, B., ... & Huang, J. (2019). Enhancing electron diffusion length in narrow-bandgap perovskites for efficient monolithic perovskite tandem solar cells. *Nature Communications*, *10*(1), 4498.

Yin, H., Xian, Y., Zhang, Y., Li, W., & Fan, J. (2019). Structurally stabilizing and environment friendly triggers: Double-metallic lead-free perovskites. *Solar Rrl*, *3*(9), 1900148.

Yu, Y., Zhao, D., Grice, C. R., Meng, W., Wang, C., Liao, W., ... & Yan, Y. (2016). Thermally evaporated methylammonium tin triiodide thin films for lead-free perovskite solar cell fabrication. *RSC Advances*, *6*(93), 90248-90254.

Zhao, S., Cai, W., Wang, H., Zang, Z., & Chen, J. (2021). All-inorganic lead-free perovskite (-like) single crystals: Synthesis, properties, and applications. *Small Methods*, *5*(5), 2001308.

Zhao, X. H., Wei, X. N., Tang, T. Y., Gao, L. K., Xie, Q., Lu, L. M., & Tang, Y. L. (2021). First-principles study on the structural, electronic and optical properties of vacancy-ordered double perovskites Cs2PtI6 and Rb2PtI6. *Optical Materials*, *114*, 110952.

Zheng, Z., Wang, S., Hu, Y., Rong, Y., Mei, A., & Han, H. (2022). Development of formamidinium lead iodide-based perovskite solar cells: Efficiency and stability. *Chemical Science*, *13*(8), 2167-2183.

Author Information

Souheyla Mamoun
Solid State Physics Team, Theoretical Physics Laboratory,
Faculty of Sciences, A Belkaid University, Box 119, 13000,
Tlemcen, Algeria
Contact e-mail*: souhila.mamoun@univ-tlemcen.dz*

Abdelkrim El-Hasnaine Merad
Solid State Physics Team, Theoretical Physics Laboratory,
Faculty of Sciences, A Belkaid University, Box 119, 13000,
Tlemcen, Algeria

Amina Benmansour
Solid State Physics Team, Theoretical Physics Laboratory,
Faculty of Sciences, A Belkaid University, Box 119, 13000,
Tlemcen, Algeria

To cite this article:

Mamoun, S., Merad, A.E., & Benmansour, A. (2024). Simulation study of electronic band diagram engineering and electrical parameters to boost the photovoltaic performance of novel Rb_2PtI_6 double perovskite solar cell. *The Eurasia Proceedings of Science, Technology, Engineering & Mathematics (EPSTEM), 32,* 389-399.